

# 1 Assessment of Simulated Soil Moisture from WRF Noah, Noah-MP, 2 and CLM Land Surface Schemes for Landslide Hazard Application

3 Lu Zhuo<sup>1</sup>, Qiang Dai<sup>1,2\*</sup>, Dawei Han<sup>1</sup>, Ningsheng Chen<sup>3</sup>, Binru Zhao<sup>1,4</sup>

4 <sup>1</sup>WEMRC, Department of Civil Engineering, University of Bristol, Bristol, UK

5 <sup>2</sup>Key Laboratory of VGE of Ministry of Education, Nanjing Normal University, Nanjing, China

6 <sup>3</sup>The Institute of Mountain Hazards and Environment (IMHE), China

7 <sup>4</sup>College of Water Conservancy and Hydropower Engineering, Hohai University, Nanjing, China

8 \*Correspondence: [civengwater@gmail.com](mailto:civengwater@gmail.com)

## 9 Abstract

10 This study assesses the usability of Weather Research and Forecasting (WRF) model simulated  
11 soil moisture for landslide monitoring in the Emilia Romagna region, northern Italy during the 10-  
12 year period between 2006 and 2015. Particularly three advanced Land Surface Model (LSM)  
13 schemes (i.e., Noah, Noah-MP and CLM4) integrated with the WRF are used to provide detailed  
14 multi-layer soil moisture information. Through the temporal evaluation with the single-point in-  
15 situ soil moisture observations, Noah-MP is the only scheme that is able to simulate the large soil  
16 drying phenomenon close to the observations during the dry season, and it also has the highest  
17 correlation coefficient and the lowest *RMSE* at most soil layers. The evaluation of the WRF rainfall  
18 estimation shows there is no distinct difference among the three LSMs, and their performances are  
19 in line with a published study for the central USA. Each simulated soil moisture product from the  
20 three LSM schemes is then used to build a landslide prediction model, and within each model, 17  
21 different exceedance probably levels from 1% to 50% are adopted to determine the optimal  
22 threshold scenario (in total there are 612 scenarios). Slope degree information is also used to  
23 separate the study region into different groups. The threshold evaluation performance is based on  
24 the landslide forecasting accuracy using 45 selected rainfall events between 2014-2015.  
25 Contingency tables, statistical indicators, and Receiver Operating Characteristic analysis for

26 different threshold scenarios are explored. The results have shown that, for landslide monitoring,  
27 Noah-MP at the surface soil layer with 30% exceedance probability provides the best landslide  
28 monitoring performance, with its hitting rate at 0.769, and its false alarm rate at 0.289.

29 **Keywords:** Emilia Romagna, Weather Research and Forecasting (WRF) Model, Land Surface  
30 Model (LSM), Numerical Weather Prediction (NWP) model, landslide hazards, soil moisture.

### 31 **1. Introduction**

32 Landslide is a repeated geological hazard during rainfall seasons, which causes massive  
33 destructions, loss of lives, and economic damages worldwide (Klose et al., 2014). The accurate  
34 predicting and monitoring of the spatiotemporal occurrence of the landslide is the key to prevent/  
35 reduce casualties and damages to properties and infrastructures. One of the most widely adopted  
36 methods for landslide prediction is based on rainfall threshold, which relies on building the rainfall  
37 intensity-duration curve using the information from the past landslide events (Chae et al., 2017).  
38 However, such a method in many cases is insufficient for landslide hazard assessment (Posner and  
39 Georgakakos, 2015), because in addition to rainfall, initial soil moisture condition is one of the  
40 main triggering factors of the events (Glade et al., 2000; Crozier, 1999; Tsai and Chen, 2010; Hawke  
41 and McConchie, 2011; Bittelli et al., 2012; Segoni et al., 2018b; Valenzuela et al., 2018; Bogaard  
42 and Greco, 2018).

43 For landslide applications, one potential soil moisture estimation method is through satellite  
44 remote sensing technologies. Although such technologies have been improved significantly over  
45 the past decade, their retrieving accuracy is still largely affected by frozen soil conditions (Zhuo  
46 et al., 2015a), and dense vegetation coverages particularly in mountainous regions (Temimi et al.,  
47 2010); furthermore, the acquired data only covers the top few centimetres of soil. Although the

48 more recently launched satellites such as Sentinel-1 (1 km, and 3 days resolution) has shown some  
49 promising performance of soil moisture estimation, its availability only covers the recent years.  
50 Those disadvantages restrict the full utilisation of satellite soil moisture products for landslide  
51 monitoring application as discussed in our previous study (Zhuo et al., 2019). In (Zhuo et al., 2019),  
52 it is discussed that both the temporal and spatial resolutions of the ESA CCI satellite soil moisture  
53 product (Dorigo et al., 2017) is too coarse for landslide applications, and its data are mostly only  
54 available after the year 2002. Moreover, the shallow depth soil moisture observation from the  
55 satellite hinders the accuracy of landslide predictions. Therefore, other alternative soil moisture  
56 estimation methods need to be explored.

57 One emerging area relies on modelling. Some studies have used modelled soil moisture data for  
58 landslide applications (Ponziani et al., 2012; Ciabatta et al., 2016; Zhao et al., 2019a; Zhao et al.,  
59 2019b). However, to our knowledge, there is a lack of existing study using the state-of-the-art  
60 Land Surface Models (LSMs) modelled soil moisture for landslide studies, such as the Noah LSM  
61 (Ek et al., 2003) and the Community Land Model (CLM) (Oleson et al., 2010). LSMs describe the  
62 interactions between the atmosphere and the land surface by simulating exchanges of momentum,  
63 heat and water within the Earth system (Maheu et al., 2018). They are capable of simulating the  
64 most important subsurface hydrological processes (e.g., soil moisture) and can be integrated with  
65 the advanced Numerical Weather Prediction (NWP) system like WRF (Weather Research and  
66 Forecasting) (Skamarock et al., 2008) for comprehensive soil moisture estimations (i.e., through  
67 the surface energy balance, the surface layer stability and the water balance equations) (Greve et  
68 al., 2013). NWP-based (i.e., with integrated LSM, thereafter) soil moisture estimations have many  
69 advantages, for instance their spatial and temporal resolution can be set at different scales  
70 depending on the input datasets to fit various application requirements; their coverage is global,

71 and the estimated soil moisture data covers multiple soil layers (from the shallow surface layer to  
72 deep root-zones); as well as a number of globally-covered data products can provide the necessary  
73 boundary and initial conditions for running the models. Soil moisture estimated through such an  
74 approach has been widely recognised and demonstrated in many studies, which cover a broad  
75 range of applications from hydrological modelling (Srivastava et al., 2013a;Srivastava et al., 2015),  
76 drought studies (Zaitchik et al., 2013), flood investigations (Leung and Qian, 2009), to regional  
77 weather prediction (Stéfanon et al., 2014). Therefore, NWP-based soil moisture datasets could  
78 provide valuable information for landslide applications. However, to our knowledge, relevant  
79 research has never been carried out.

80 The aim of this study hence is to evaluate the usefulness of NWP modelled soil moisture for  
81 landslide monitoring. Here the advanced WRF model (version 3.8) is adopted, because it offers  
82 numerous physics options such as micro-physics, surface physics, atmospheric radiation physics,  
83 and planetary boundary layer physics (Srivastava et al., 2015), and can integrate with a number of  
84 LSM schemes, each varying in physical parameterisation complexities. So far there is limited  
85 literature in comparing the soil moisture accuracy of different LSMs options in the WRF model.  
86 Therefore, in this study, we select three of the WRF's most advanced LSM schemes (i.e., Noah,  
87 Noah-Multiparameterization (Noah-MP), and CLM4) to compare their soil moisture performance  
88 for landslide hazard assessment. Furthermore, since all the three schemes can provide multi-layer  
89 soil moisture information, it is useful to include all those simulations for the comparison so that  
90 the optimal depth of soil moisture could be determined for the landslide monitoring application.  
91 In order to compare with the performance of our previous study on using the satellite soil moisture  
92 data (Zhuo et al., 2019), the same study area called Emilia Romagna is used here. The study period  
93 covers 10 years from 2006 to 2015 to include a long-term record of landslide events. In addition,

94 because slope angle is one of the major factors controlling the stability of the slope, it is hence  
95 used in this study to divide the study area into several slope groups, so that a more accurate  
96 landslide prediction model could be built.

97 The description of the study area and the used datasets are included in Section 2. Methodologies  
98 regarding the WRF model, the related LSM schemes and the adopted landslide threshold  
99 evaluation approach are provided in Section 3. Section 4 shows the WRF soil moisture evaluation  
100 results against the in-situ observations, and the WRF rainfall evaluations over the whole study area.  
101 Section 5 covers the comparison results of the WRF modelled soil moisture products for landslide  
102 applications. The discussion and conclusion of the study are included in Section 6.

## 103 **2. Study Area and Datasets**

### 104 **2.1 Study Area**

105 The study area is in the Emilia Romagna Region, northern Italy (Figure 1). Its population density  
106 is high. The region has high mountainous areas in the S-SW, and wide plain areas towards NE,  
107 with a large elevation difference (i.e., 0 m to 2125 m) across 50 km distance from the north to the  
108 south (Rossi et al., 2010). The region has a mild Mediterranean climate with distinct wet and dry  
109 seasons (i.e., dry season between May and October, and wet season between November and April).  
110 The study area tends to be affected by landslide events easily, with approximately one-fifth of the  
111 mountainous zone covered by active or dormant landslide deposits (Bertolini et al., 2005). Rainfall  
112 is by far the primary triggering factor of landslides in the region, followed by snow melting:  
113 shallow landslides are mainly triggered by short but exceptionally intense rainfall, and long and  
114 moderate rainfall events over saturated conditions, while deep-seated landslides have a more  
115 complex response to rainfall and are mainly caused by moderate but exceptionally prolonged (even

116 up to 6 months) periods of rainfalls (Segoni et al., 2015). Due to the abundant data available in the  
117 region, several studies on regional scale landslide prediction and early warning have been  
118 published (Berti et al., 2012;Martelloni et al., 2012;Lagomarsino et al., 2015;Segoni et al.,  
119 2018b;Segoni et al., 2018a;Lagomarsino et al., 2013). Interested readers can refer to those studies  
120 for more information.

## 121 **2.2 Selection of The Landslide Events**

122 The landslides catalog is collected from the Emilia Romagna Geological Survey (Berti et al., 2012).  
123 The information included in the catalog are: location, date of occurrence, the uncertainty of date,  
124 landslide characteristics (dimensions, type, and material), triggering factors, damages, casualties,  
125 and references. Unfortunately, many pieces of the information are missing from the records in  
126 many cases. In order to organise the data in a more systematic way so that only the relevant events  
127 are retained, a two-step event selection procedure is initially carried out based on: 1) rainfall-  
128 induced only; and 2) high spatial-temporal accuracy (exact date and coordinates). Finally, a  
129 revision of the information about the type of slope instabilities such as landslide/debris  
130 flow/rockfall and the characteristics of the affected slope (natural or artificial) is also carried out  
131 over the selected records (Valenzuela et al., 2018). The catalog period used in this study covers  
132 between 2006 and 2015, which is in accordance with the WRF model run. After filtering the data  
133 records, only one-fifth of them (i.e., 157 events) is retained. The retained events are shown as  
134 single circles in Figure 2, with slope information (calculated through the Digital Elevation Model  
135 (DEM) data) also presented in the background. It can be seen the spatial distribution of the  
136 occurred landslide events is very heterogeneous, with nearly all of them occurred in the hilly  
137 regions.

## 138 **2.3 Datasets**

139 There is a total of 19 soil moisture stations available within the study area, however, based on our  
140 collected data, only one of them at the San Pietro Capofiume (latitude 44° 39' 13.59", longitude  
141 11° 37' 21.6") provides long-term valid soil moisture retrievals (i.e., 2006 to 2017). We have  
142 checked the data from all the rest of the stations, they are either absent (or have very big data gaps)  
143 or do not cover the research period at all. Therefore, only the San Pietro Capofiume station is used  
144 for the WRF soil moisture temporal evaluation. The soil moisture is measured from 10 cm to 180  
145 cm deep in the soil at 5 depths, by the Time Domain Reflectometry (TDR) instrument. Data are  
146 recorded in the unit of volumetric water content ( $m^3/m^3$ ) and at daily timestep (Pistocchi et al.,  
147 2008). The data used in this study is between 2006 and 2015. Rainfall data over the whole study  
148 area is collected from over 200 tipping-bucket rain gauges, which are used to assess the quality of  
149 the WRF model's rainfall estimations in the study area, as well as for rainfall events selection  
150 during the Year 2014 and 2015.

151 To drive a NWP model like WRF for soil moisture simulations, several globally-coved data  
152 products can be chosen for extracting the boundary and initial conditions information, for instance,  
153 the European Centre for Medium-Range Weather Forecasts (ECMWF) reanalysis (ERA-Interim)  
154 and the National Centre for Environmental Prediction (NCEP) reanalysis are two of the most  
155 commonly used data products. It has been found by (Srivastava et al., 2013b) that the ERA-Interim  
156 datasets can provide better boundary conditions than the NCEP datasets for WRF hydro-  
157 meteorological predictions in Europe, which is therefore adopted in this study to drive the WRF  
158 model. The spatial resolution of the ERA-Interim is approximately 80 km. The data is available  
159 from 1979 to present, containing 6-hourly gridded estimates of three-dimensional meteorological  
160 variables, and 3-hourly estimates of a large number of surface parameters and other two-

161 dimensional fields. A comprehensive description of the ERA-Interim datasets can be found in (Dee  
162 et al., 2011)

163 The Shuttle Radar Topography Mission (SRTM) 3 Arc-Second Global (~ 90m) DEM datasets are  
164 downloaded and used as the basis for the slope degree calculations. SRTM DEM data has been  
165 widely used for elevation-related studies worldwide due to its high quality, near-global coverage,  
166 and free availability (Berry et al., 2007).

### 167 **3. Methodologies**

#### 168 **3.1 WRF Model and The Three Land Surface Model Schemes**

169 The WRF model is a next-generation, non-hydrostatic mesoscale NWP system designed for both  
170 atmospheric research and operational forecasting applications (Skamarock et al., 2005). The model  
171 is powerful enough in modelling a broad range of meteorological applications varying from tens  
172 of metres to thousands of kilometres (NCAR, 2018). It has two dynamical solvers: the ARW  
173 (Advanced Research WRF) core and the NMM (Nonhydrostatic Mesoscale Model) core. The  
174 former has more complex dynamic and physics settings than the latter which only has limited  
175 setting choices. Hence in this study WRF with ARW dynamic core (version 3.8) is used to perform  
176 all the soil moisture simulations.

177 The main task of LSM within the WRF is to integrate information generated through the surface  
178 layer scheme, the radiative forcing from the radiation scheme, the precipitation forcing from the  
179 microphysics and convective schemes, and the land surface conditions to simulate the water and  
180 energy fluxes (Ek et al., 2003). WRF provides several LSM options, among which three of them  
181 are selected in this study as mentioned in the introduction: Noah, Noah-MP, and CLM4. Table 1  
182 gives a simple comparison of the three models. The detailed description of the models is written



183 below in the order of increasing complexity in regards of the way they deal with thermal and  
184 moisture fluxes in various layers of soil, and their vegetation, root and canopy effects  
185 (Skamarock et al., 2008).

### 186 **3.1.1 Noah**

187 Noah is the most basic amongst the three selected LSMs. It is one of the ‘second generation’ LSMs  
188 that relies on both soil and vegetation processes for water budgets and surface energy closures  
189 (Wei et al., 2010). The model is capable of modelling soil and land surface temperature, snow  
190 water equivalent, as well as the general water and energy fluxes. The model includes four soil  
191 layers that reach a total depth of 2 m in which soil moisture is calculated. Its bulk layer of canopy  
192 -snow-soil (i.e., lack the abilities in simulating photosynthetically active radiation (PAR),  
193 vegetation temperature, correlated energy, and water, heat and carbon fluxes), ‘leaky’ bottom (i.e.,  
194 drained water is removed immediately from the bottom of the soil column which can result in  
195 much fewer memories of antecedent weather and climate fluctuations) and simple snow melt-thaw  
196 dynamics are seen as the model’s demerits (Wharton et al., 2013). Noah calculates the soil moisture  
197 from the diffusive form of Richard’s equation for each of the soil layer (Greve et al., 2013), and  
198 the evapotranspiration from the Ball-Berry equation (considering both the water flow mechanism  
199 within soil column and vegetation, as well as the physiology of photosynthesis (Wharton et al.,  
200 2013)).

### 201 **3.1.2 Noah-MP**

202 Noah-MP (Niu et al., 2011) is an improved version of the Noah LSM, in the aspect of better  
203 representations of terrestrial biophysical and hydrological processes. Major physical mechanism  
204 improvements directly relevant to soil water simulations include: 1) introducing a more permeable

205 frozen soil by separating permeable and impermeable fractions (Cai, 2015), 2) adding an  
206 unconfined aquifer immediately beneath the bottom of the soil column to allow the exchange of  
207 water between them (Liang et al., 2003), and 3) the adoption of a TOPMODEL (TOPography  
208 based hydrological MODEL)-based runoff scheme (Niu et al., 2005) and a simple SIMGM  
209 groundwater model (Niu et al., 2007) which are both important in improving the modelling of soil  
210 hydrology. Noah-MP is unique compared with the other LSMs, as it is capable of generating  
211 thousands of parameterisation schemes through the different combinations of “dynamic leaf,  
212 canopy stomatal resistance, runoff and groundwater, a soil moisture factor controlling stomatal  
213 resistance (the  $\beta$  factor), and six other processes” (Cai, 2015). The scheme option used in the study  
214 are: Ball-Berry scheme for canopy stomatal resistance, Monin-Obukhov scheme for surface layer  
215 drag coefficient calculation, the Noah based soil moisture factor for stomatal resistance, the  
216 TOPMODEL runoff with the SIMGM groundwater, the linear effect scheme for soil permeability,  
217 the two-stream applied to vegetated fraction scheme for radiative transfer, the CLASS (Canadian  
218 Land Surface Scheme) scheme for ground surface albedo option, and the Jordan (Jordan, 1991)  
219 scheme for partitioning precipitation between snow and rain.

### 220 **3.1.3. CLM4**

221 CLM4 is developed by the National Center for Atmospheric Research (NCAR) to serve as the land  
222 component of its Community Earth System Model (formerly known as the Community Climate  
223 System Model) (Lawrence et al., 2012). It is a ‘third generation’ model that incorporates the  
224 interactions of both nitrogen and carbon in the calculations of water and energy fluxes. Compared  
225 with its previous versions, CLM4 (Oleson et al., 2008) has multiple enhancements relevant to soil  
226 moisture computing. For instance, the model’s soil moisture is estimated by adopting an improved  
227 one-dimensional Richards equation (Zeng and Decker, 2009); the new version allows the dynamic

228 interchanges of soil water and groundwater through an improved definition of the soil column's  
229 lower boundary condition that is similar to the Noah-MP's (Niu et al., 2007). Furthermore, the  
230 thermal and hydrologic properties of organic soil are included for the modelling which is based on  
231 the method developed in (Lawrence and Slater, 2008). The total ground column is extended to 42  
232 m depth, consisting 10 soil layers unevenly spaced between the top layer (0.0–1.8 cm) and the  
233 bottom layers (229.6–380.2 cm), and 5 bedrock layers to the bottom of the ground column  
234 (Lawrence et al., 2011). Soil moisture is estimated for each soil layer.

### 235 **3.2 WRF Model Parameterization**

236 The WRF model is centred over the Emilia Romagna Region with three nested domains (D1, D2,  
237 D3 with the horizontal grid sizes of 45 km, 15 km, and 5 km, respectively), of which the innermost  
238 domain (D3, with 88 x 52 grids (west-east and south-north, respectively)) is used in this study. A  
239 two-way nesting scheme is adopted allowing information from the child domain to be fed back to  
240 the parent domain. With atmospheric forcing, static inputs (e.g., soil and vegetation types), and  
241 parameters, the WRF model needs to be spin-up to reach its equilibrium state before it can be used  
242 (Cai et al., 2014;Cai, 2015). In this study, WRF is spin-up by running through the whole year of  
243 2005. After the spin-up, the WRF model for each of the selected LSM scheme is executed in daily  
244 timestep from January 1, 2006, to December 31, 2015, using the ERA-Interim datasets.

245 The microphysics scheme plays a vital role in simulating accurate rainfall information which in  
246 turn is important for modelling the accurate soil moisture variations. WRF V3.8 is supporting 23  
247 microphysics options range from simple to more sophisticated mixed-phase physical options. In  
248 this study, the WRF Single-Moment 6-class scheme is adopted which considers ice, snow and  
249 graupel processes and is suitable for high-resolution applications (Zaidi and Gisen, 2018). The  
250 physical options used in the WRF setup are Dudhia shortwave radiation (Dudhia, 1989) and Rapid

251 Radiative Transfer Model (RRTM) longwave radiation (Mlawer et al., 1997). Cumulus  
252 parameterization is based on the Kain-Fritsch scheme (Kain, 2004) which is capable of  
253 representing sub-grid scale features of the updraft and rain processes, and such a capability is  
254 beneficial for real-time modelling (Gilliland and Rowe, 2007). The surface layer parameterization  
255 is based on the Revised fifth-generation Pennsylvania State University–National Center for  
256 Atmospheric Research Mesoscale Model (MM5) Monin-Obukhov scheme (Jiménez et al., 2012).  
257 The Yonsei University scheme (Hong et al., 2006) is selected to calculate the planetary boundary  
258 layer. The parameterization schemes used in the WRF modelling are shown in Table 2. The  
259 datasets for land use and soil texture are available in the pre-processing package of WRF. In this  
260 study, the land use categorisation is interpolated from the MODIS 21-category data classified by  
261 the International Geosphere Biosphere Programme (IGBP). The soil texture data are based on the  
262 Food and Agriculture Organization of the United Nations Global 5-minutes soil database.

### 263 **3.3 Translation of Observed and Simulated Soil Moisture Data to Common Soil Layers**

264 Since all soil moisture datasets have different soil depths, it is difficult for a direct comparison.  
265 The Noah and Noah-MP models include four soil layers, centred at 5, 25, 70, and 150 cm,  
266 respectively. Whereas CLM4 model has 10 soil layers, centered at 0.9, 3.2, 6.85, 12.85, 22.8, 39.2,  
267 66.2, 110.65, 183.95, 304.9 cm, respectively. Moreover, the in-situ sensor measures soil moisture  
268 centred at 10, 25, 70, 135, and 180 cm. In order to make the datasets comparable at consistent soil  
269 depths, the simple linear interpolation approach described in (Zhuo et al., 2015b) is applied in this  
270 study, and a benchmark of the soil layer centred at 10, 25, 70 and 150 cm is adopted.

### 271 **3.4 Soil Moisture Thresholds Build Up and Evaluations**

272 To build and evaluate the soil moisture thresholds for landslides forecasting, all datasets have been  
273 grouped into two portions: 2006-2013 for the establishment of thresholds, and 2014-2015 for the  
274 evaluation. The determination of soil moisture thresholds is based on determining the most suitable  
275 soil moisture triggering level for landslides occurrence by trying a range of exceedance  
276 probabilities (percentiles). For example, a 10% exceedance probability is calculated by  
277 determining the 10% percentile result of the soil moisture datasets that are related to the occurred  
278 landslides. The exceedance probability method is commonly utilised in landslide early warning  
279 studies for calculating the rainfall-thresholds, which is therefore adopted here to examine its  
280 performance for soil moisture threshold calculations.

281 To carry out the threshold evaluation, 45 rainfall events (during 2014-2015) are selected for the  
282 purpose. The rainfall events are separated based on at least one-day of dry period (i.e., a period  
283 without rainfall). The rainfall data from each rain gauge station is firstly combined using the  
284 Thiessen Polygon method, and with visual analysis, the 45 events are then finally selected. The  
285 information about the selected rainfall events can be found in Section 5. The threshold evaluation  
286 is based on the statistical approach described in (Gariano et al., 2015;Zhuo et al., 2019), where soil  
287 moisture threshold can be treated as a binary classifier of the soil moisture conditions that are likely  
288 or unlikely to cause landslide events. With this hypothesis, the likelihood of a landslide event can  
289 either be *true (T)* or *false (F)*, and the threshold forecasting can either be *positive (P)* or *negative*  
290 *(N)*. The combinations of those four conditions can lead to four statistical outcomes (Figure 3a)  
291 that are: *true positive (TP)*, *true negative (TN)*, *false positive (FP)*, and *false negative (FN)* (Wilks,  
292 2011). Using the four outcomes, two statistical scores can be determined.

293 The Hit Rate (*HR*), which is the rate of the events that are correctly forecasted. Its formula is:

$$294 \quad HR = \frac{TP}{TP+FN} \quad (1)$$

295 in the range of 0 and 1, with the best result as 1.

296 The False Alarm Rate (*FAR*), which is the rate of false alarms when the event did not occur. Its  
297 formula is:

$$298 \quad FAR = \frac{FP}{FP+TN} \quad (2)$$

299 in the range of 0 and 1, with the best result as 0.

300 For any soil moisture product, each threshold calculated is adopted to determine *T*, *F*, *P*, and *N*,  
301 respectively. Those values are finally integrated to find the overall scores of *TP*, *FN*, *FP*, *TN*, *HR*,  
302 and *FAR*. The threshold performance is then judged via the Receiver Operating Characteristic  
303 (ROC) analysis (Hosmer and Lemeshow, 1989; Fawcett, 2006). As shown in Figure 3b, ROC curve  
304 is based on *HR* against *FAR*, and each point in the curve represents a threshold scenario (i.e.,  
305 selected exceedance probabilities). The optimal result (the red point) can only be realised when  
306 the *HR* reaches 1 and the *FAR* reduces to 0. The closer the point to the red point, the better the  
307 forecasting result is. To analyse and compare the forecasting performance numerically, the  
308 Euclidean distances (*d*) for each scenario to the optimal point are computed.

#### 309 **4. WRF Model Evaluations**

310 In this study, the evaluation is based on the daily mean soil moisture. The reason for not using the  
311 antecedent soil moisture condition plus rainfall data on the day is because the purpose of this study  
312 is to explore the relationship between different WRF simulated soil moisture and landslides solely.  
313 In general, soil moisture is a predisposing factor for slope instability, while rainfall is the triggering  
314 factor. The same rainfall may trigger or not a landslide depending on the soil moisture content at  
315 the time of the rainfall event. The mean soil moisture on the day of the landslide implicitly account  
316 for both the initial soil moisture and the effective rainfall absorbed by the ground, and can be a  
317 robust indicator of the hydrological condition of the slope.

#### 318 4.1 Soil Moisture Temporal Comparisons

319 Although there is only one soil moisture sensor that provides long-term soil moisture data in the  
320 study region, it is still useful to compare it with the WRF estimated soil moisture. In this study, we  
321 carry out a temporal comparison between all the three WRF soil moisture products with the in-situ  
322 observations. The comparison is implemented over the period from 2006 to 2015, and the WRF  
323 grid closest to the in-situ sensor location is chosen. Figure 4 shows the comparison results at the  
324 four soil depths. The statistical performance (correlation coefficient  $r$  and Root Mean Square Error  
325  $RMSE$ ) of the three LSM schemes are summarised in Table 3. Based on the statistical results,  
326 Noah-MP surpasses other schemes at most soil layers, except for Layer 2 where CLM4 shows  
327 stronger correlation and Layer 4 where Noah gives smaller  $RMSE$  error. For Noah-MP, the best  
328 correlation is observed at the surface layer (0.809), followed by the third (0.738), second (0.683)  
329 and fourth (0.498) layers; and based on  $RMSE$ , the best performance is again observed at the  
330 surface layer and followed by the second, third and fourth layers in sequence (as 0.060, 0.070,  
331 0.088, and 0.092  $m^3/m^3$ , respectively). From the temporal plots, it can be seen at all four soil layers,  
332 all three LSM schemes can produce the soil moisture's seasonal cycle with most upward and  
333 downward trends successfully represented. However, both the Noah and the CLM4 overestimate  
334 the variability at the upper two soil layers during almost the whole study period, and the situation  
335 is the worst for the Noah. Comparatively, the Noah-MP can better capture the wet soil moisture  
336 conditions especially at the surface layer; and it is the only model of the three that is able to  
337 simulate the large soil drying phenomenon close to the observations during the dry season, except  
338 for some extremely dry days. Towards 70 cm depth, although Noah-MP is still able to capture  
339 most of the soil moisture variabilities during the drying period, it significantly underestimates soil  
340 moisture values for most wet days. Similar underestimation results can be observed for CLM4 and

341 Noah during the wet season at 70 cm; furthermore, both schemes are again not capable of  
342 reproducing the extremely drying phenomenon and overestimate soil moisture for most of the dry  
343 season days. It is surprising to see that at the deep soil layer (150 cm), all soil moisture products  
344 are underestimated, in particular, the outputs from the CLM4 and the Noah-MP only show small  
345 fluctuations. However, the soil moisture measurements from the in-situ sensor also get our  
346 attention as they show strange fluctuations with numerous sudden drops and rise situations  
347 observed. The strange phenomenon is not expected at such a deep soil layer (although groundwater  
348 capillary forces can increase the soil moisture, its rate is normally very slow). One possible reason  
349 we suspect is due to sensor failure in the deep zone. Therefore, the assessment result for the deep  
350 soil layer should be considered unreliable. Overall for the Noah-MP, in addition to producing the  
351 highest correlation coefficient and the lowest *RMSE*, its simulated soil moisture variations are the  
352 closest to the observations. The better performance of the Noah-MP over the other two models  
353 agrees with the results found in (Cai et al., 2014) (note: the paper uses standalone models, which  
354 are not coupled with WRF). Also, it has been discussed in (Yang et al., 2011), the Noah MP  
355 presents a clear improvement over the Noah in simulating soil moisture globally. However, it is  
356 noted the evaluation results are only based on one soil moisture sensor located at the plain part of  
357 the study area.

## 358 **4.2 Rainfall Evaluations**

359 Since soil moisture is related to rainfall, it is useful to carry out the evaluations of WRF rainfall  
360 estimations against the observations in the study area. The spatial plot of *R* for the three LSMs is  
361 shown in Figure 5. It can be seen the performance of the three models are very close to each other,  
362 with only small differences over the whole study region. In general, the performance is the best in  
363 the Southeast region, with *R* reaches above 0.70. The poorest performance is observed in the



364 Northeast region and some parts of the mountain zone. Based on the spatial distribution of  $R$ , there  
365 is no clear correlation between the WRF rainfall performance and the topography of the region.  
366 The boxplot for the  $R$  performance is illustrated in Figure 6a. It can be seen again the performances  
367 of the three models are very similar. Generally,  $R$  ranges between around 0.10 and 0.80, and with  
368 the majority of the region performs around 0.40.  $RMSE$  performance is also calculated. Similar to  
369 the results of  $R$ , it has been found the  $RMSE$  spatial distributions are very similar among the three  
370 models. Therefore, the  $RMSE$  spatial distribution map is not included in this paper. The boxplot of  
371 the  $RMSE$  is shown in Figure 6b. Generally, the  $RMSE$  ranges between around 4 mm and 12 mm,  
372 with some outliers between around 12 mm and 20 mm. Majority of the region performs at around  
373 7 mm  $RMSE$ . The statistical calculations are summarised in Table 4. Based on the results of  $R$  and  
374  $RMSE$ , the WRF rainfall estimation performance in Emilia is similar to the one found in central  
375 USA (Van Den Broeke et al., 2018).

## 376 **5. The Assessment of WRF Soil Moisture Threshold for Landslide Monitoring**

377 As introduced at the beginning of the paper, previous works have demonstrated that in complex  
378 geomorphologic settings (e.g., in Emilia Romagna), a rainfall threshold approach is too simple and  
379 more hydrologically driven approaches need to be established. This section is to assess if the spatial  
380 distribution of soil moisture can provide useful information for landslide monitoring at the regional  
381 scale. Particularly, all three soil moisture products simulated through the WRF model are used to  
382 derive threshold models, and the corresponding landslide prediction performances are then  
383 compared statistically. Here the threshold is defined as the crucial soil moisture condition above  
384 which landslides are likely to happen.

385 Among different factors for controlling the stability of slope, the slope angle is one of the most  
386 critical ones. From the slope angle map in Figure 2, it can be seen the region has a clear spatial

387 pattern of high and low slope areas, with the majority of the high-slope areas (can be as steep as  
388 around 40 degrees) located in the mountainous Southern part and the river valleys. Based on the  
389 analysed events data, the landslides happened during the study period are mainly located in the  
390 high-slope region, with a particularly high concentration around the central Southern part. The  
391 spatial distribution of the landslide events is also in line with the overall geological characteristics  
392 of the region, i.e., the Southern part mainly constitutes outcrop of sandstone rocks that make up  
393 the steep slopes and are covered by a thin layer of permeable sandy soil, which are highly unstable.  
394 Therefore, instead of only using one soil moisture threshold for the whole study area, it is useful  
395 to divide the region into several slope groups so that within each group a threshold model is built.  
396 To derive soil moisture threshold individually under different slope conditions, all data has been  
397 divided into three groups based on the slope angle ( $0.4-1.86^{\circ}$ ;  $1.87-9.61^{\circ}$ ;  $9.52-40.43^{\circ}$ ; since no  
398 landslide events are recorded under the  $0-0.39^{\circ}$  group, the group is not considered here), as results,  
399 all groups have equal coverage areas. There are different ways to group the slopes. In this study,  
400 three groups have been defined with similar sizes so that relatively reliable results could be  
401 achieved from the statistical point of view.

402 In order to find the optimal threshold so that there are least missing alarms (i.e., threshold is  
403 overestimated) and false alarms (i.e., threshold is underestimated), we test out 17 different  
404 exceedance probabilities from 1% to 50%. For each LSM scheme, the total number of threshold  
405 models is 204, which is the resultant of different combinations of slope groups, soil layers, and  
406 exceedance probability conditions. The calculated thresholds for all LSM schemes under three  
407 slope groups are plotted in Figure 7. Overall there is a clear trend between the slope angle and the  
408 soil moisture threshold, that is with threshold becoming smaller for steeper areas. The correlation  
409 is more evident at the upper three soil layers (i.e., the top 1 m depth of soil), with only a few

410 exceptions for Noah and CLM4 at the 1% and the 2% exceedance probabilities. At the deep soil  
411 layer centred at 150 cm, the soil moisture threshold difference between Slope Group (S.G.) 2 and  
412 3 becomes very small for all the three LSM schemes. This could be partially because at the deep  
413 soil layer, the change of soil moisture is much smaller than at the surface layer, therefore the soil  
414 moisture values for S.G. 2 and 3 could be too similar to differentiate. However, for milder slopes  
415 (S.G. 1), the higher soil moisture triggering level always applies even down to the deepest soil  
416 layer for all the three LSM schemes. In this study, the results show that wetter soil can trigger  
417 landslides easier in milder slopes than in steeper slopes.

418 All the threshold models are then evaluated under the 45 selected rainfall events (Table 5) using  
419 the ROC analysis. Each threshold determined for each of the slope class during the calibration is  
420 used for the evaluation. The period of the selected rainfall events is between 1 day and 18 days,  
421 and the average rainfall intensity ranges from 5.05 mm/day to 24.69 mm/day. The resultant  
422 Euclidean distances ( $d$ ) between each scenario of exceedance probability and the optimal point for  
423 ROC analysis are listed in Table 6 for all three WRF LSM schemes at the tested exceedance  
424 probabilities. The best performance (i.e., lowest  $d$ ) in each column (i.e., each soil layer of an LSM  
425 scheme) is highlighted. In addition, the  $d$  results are also plotted in Figure 8 to give a better view  
426 of the overall trend amongst different soil layers and LSM schemes. From the figure, for all three  
427 LSM schemes at all four soil layers, there is an overall downward and then stabilised trend. Overall  
428 for Noah, the simulated surface layer soil moisture provides better landslide monitoring  
429 performance than the rest of the soil layers from 1% to 35% exceedance probabilities; and the  
430 scheme's worst performance is observed at the third soil layer centred at 70 cm. The values of  $d$   
431 for Noah's second and fourth layer are quite close to each other. For Noah-MP, the simulated  
432 surface layer soil moisture gives the best performance amongst all four soil layers for most cases

433 between the 1% and 35% exceedance probability range; and the scheme's worst performance is  
434 observed at the fourth layer. Unlike Noah, all four soil layers from the Noah-MP scheme provide  
435 distinct performance amongst them (i.e., larger  $d$  difference). For CLM4, the performance for the  
436 surface layer is quite similar to the second layer's, and the differences between the four layers are  
437 small. From the Table 6, it can be seen for Noah the most suitable exceedance probabilities (i.e.,  
438 the highlighted numbers) range between 35% to 50%; for Noah-MP they are between 30% and  
439 50%, and for CLM4 it stays at 40% for all four soil layers. For both Noah and Noah-MP, the best  
440 performance is observed at the surface layer ( $d = 0.392$  and  $d = 0.369$ , respectively). Furthermore,  
441 the best performance for Noah and Noah-MP follows a regular trend, that is the deeper the soil  
442 layer, the poorer the landslide monitoring performance. There are several potential reasons for  
443 such an outcome. First, the simulated soil moisture accuracy at the shallower layers are better than  
444 the deeper zones. Second, although the wetness conditions at the sliding surface are important, the  
445 soil moisture above it is also important (i.e., the loading should be heavier with more water in the  
446 upper soil layer). Third, the region has very shallow landslides. Fourth, the WRF modelled soil  
447 moisture is not accurate enough in assessing the landslide events in the study region. In order to  
448 find out the extract reasons, comprehensive studies with more detailed landslide events datasets  
449 are needed in future studies. For CLM4, the best performances show no distinct pattern amongst  
450 soil layers (i.e., with the best performance found at the soil layer 3, followed by layer 2, 1, and 4).  
451 Of all the LSM schemes and soil layers, the best performance is found for Noah-MP at the surface  
452 layer with 30% exceedance probability ( $d=0.369$ ). Based on the  $d$  results, WRF modelled soil  
453 moisture provides better landslide prediction performance than the satellite ESA-CCI soil moisture  
454 products as shown in our previous study ((Zhuo et al., 2019), i.e.,  $d = 0.51$ ). The ROC curve for  
455 the Noah-MP scheme at the surface layer is shown in Figure 9. In the curve, each point represents

456 a scenario with a selected exceedance probability level. It is clear with various exceedance  
457 probabilities, *FAR* can be decreased without sacrificing the *HR* score (e.g., 4% to 10% exceedance  
458 probabilities). At the optimal point at the 30% exceedance probability, the best results for *HR* and  
459 *FAR* are observed as 0.769 and 0.289, respectively.

## 460 **6. Discussions and Conclusion**

461 In this study, the usability of WRF modelled soil moisture for landslide monitoring has been  
462 evaluated in the Emilia Romagna region based on the research duration between 2006 and 2015.  
463 Specifically, four-layer soil moisture information simulated through the WRF's three most  
464 advanced LSM schemes (i.e., Noah, Noah-MP and CLM4) are compared for the purpose. Through  
465 the temporal comparison with the in-situ soil moisture observations, it has been found that all three  
466 LSM schemes at all four soil layers can produce the general soil moisture's seasonal cycle.  
467 However, only Noah-MP is able to simulate the large soil drying phenomenon close to the  
468 observations during the drying season, and it also gives the highest correlation coefficient and the  
469 lowest *RMSE* at most soil layers amongst the three LSM schemes. However, it should be noted,  
470 the soil moisture evaluation is only based on a single point-based soil moisture sensor that is  
471 available in the plain region of the study area. Therefore, the WRF soil moisture performance over  
472 the whole study region, in particular, at the mountainous zone cannot be evaluated in this study.  
473 Since soil moisture is related to rainfall, we have carried out the WRF rainfall assessments, based  
474 on the comparison with the dense rainfall network in the region. The results have shown that there  
475 is no distinct difference between the three LSM schemes. The WRF rainfall performance is found  
476 to be similar to a study carried out over the central USA. A landslide prediction model based on  
477 soil moisture and slope angle condition is built up. 17 various exceedance probably levels between  
478 1% and 50% are adopted to find the optimal threshold scenario. Through the ROC analysis of 612

479 threshold models, the best performance is obtained by the Noah-MP at the surface soil layer with  
480 30% exceedance probability.

481 It should be noted that weighting factors are not considered in the evaluation of the threshold  
482 models. Weighting factors can include both social and economic components, for instance, it can  
483 include the cost of a disaster event (e.g., both short-term and long-term impacts), the cost of the  
484 evacuation (e.g., relocation cost, business shut down), as well as the social impacts of both cases.  
485 In real-life situations, the weighting could play important roles during the final decision making.  
486 As for instance, the damages resulted from a missing alarm event could be much more devastating  
487 than a false alarm event, or vice versa, and the situation also varies in different regions. Therefore,  
488 during operational applications, appropriate weighting factors should be considered.

489 In this study, WRF is modelled based on the ERA-Interim datasets, however, it has been found in  
490 some studies, the performance of using the ERA5 has surpassed the ERA-Interim. Therefore, the  
491 ERA5 datasets will be tested in our future studies. Model-based soil moisture estimations could be  
492 affected by error accumulation issues, especially in the real-time forecasting mode. A potential  
493 solution is to use data assimilation methodologies to correct such errors by assimilating soil  
494 moisture information from other data sources. Since in-situ soil moisture sensors are only sparsely  
495 available in limited regions, soil moisture measured via satellite remote sensing technologies could  
496 provide useful alternatives. Another issue is with the landslide record data, since most of them are  
497 based on human experiences (e.g., through newspapers, and victims), a lot of incidences could be  
498 unreported. Therefore, the conclusion made here could be biased. One way of expanding the  
499 current landslide catalog can depend on automatic landslide detection methods based on remote  
500 sensing images.

501 In summary, this study provides an overview of the soil moisture performance of three WRF LSM  
502 schemes for landslide hazard assessment. Based on the results, we demonstrate that the surface  
503 soil moisture (centred at 10 cm) simulated through the Noah-MP LSM scheme is useful in  
504 predicting landslide occurrences in the Emilia Romagna region. With the hitting rate of 0.769 and  
505 the false alarm rate of 0.289 obtained in this study, such soil moisture information has the potential  
506 in working with rainfall data to provide landslide predictions. However, one must bear in mind  
507 that the results demonstrated in this study are only valid for the selected region. In order to make  
508 a general conclusion, more researches are needed using the methodology described in this paper.  
509 Particularly, a considerable number of catchments with a broad spectrum of climate and  
510 environmental conditions will need to be investigated.

#### 511 **Acknowledgement**

512 This study is supported by Resilient Economy and Society by Integrated SysTems modelling  
513 (RESIST), Newton Fund via Natural Environment Research Council (NERC) and Economic and  
514 Social Research Council (ESRC) (NE/N012143/1), and the National Natural Science Foundation  
515 of China (No: 4151101234). The Landslide inventory data is kindly provided by Dr Matteo Berti,  
516 University of Bologna.

#### 517 **References**

518 Berry, P., Garlick, J., and Smith, R.: Near-global validation of the SRTM DEM using satellite  
519 radar altimetry, *Remote Sensing of Environment*, 106, 17-27, 2007.

520 Berti, M., Martina, M., Franceschini, S., Pignone, S., Simoni, A., and Pizziolo, M.: Probabilistic  
521 rainfall thresholds for landslide occurrence using a Bayesian approach, *Journal of Geophysical*  
522 *Research: Earth Surface*, 117, 2012. DOI: <https://doi.org/10.1029/2012JF002367>.

523 Bertolini, G., Guida, M., and Pizziolo, M. J. L.: Landslides in Emilia-Romagna region (Italy):  
524 strategies for hazard assessment and risk management, 2, 302-312, 2005.

525 Bittelli, M., Valentino, R., Salvatorelli, F., and Pisa, P. R.: Monitoring soil-water and displacement  
526 conditions leading to landslide occurrence in partially saturated clays, *Geomorphology*, 173, 161-  
527 173, 2012.

528 Bogaard, T., and Greco, R.: Invited perspectives: Hydrological perspectives on precipitation  
529 intensity-duration thresholds for landslide initiation: proposing hydro-meteorological thresholds,  
530 *Natural Hazards and Earth System Sciences*, 18, 31-39, 2018.

531 Cai, X., Yang, Z. L., Xia, Y., Huang, M., Wei, H., Leung, L. R., and Ek, M. B.: Assessment of  
532 simulated water balance from Noah, Noah-MP, CLM, and VIC over CONUS using the NLDAS  
533 test bed, *Journal of Geophysical Research: Atmospheres*, 119, 13,751-713,770, 2014.

534 Cai, X.: Hydrological assessment and biogeochemical advancement of the Noah-MP land surface  
535 model, Doctor of Philosophy, Geological Sciences, The University of Texas at Austin, 164 pp.,  
536 2015.

537 Chae, B.-G., Park, H.-J., Catani, F., Simoni, A., and Berti, M.: Landslide prediction, monitoring  
538 and early warning: a concise review of state-of-the-art, *Geosciences Journal*, 21, 1033-1070, 2017.

539 Chen, F., and Dudhia, J.: Coupling an advanced land surface-hydrology model with the Penn State-  
540 NCAR MM5 modeling system. Part I: Model implementation and sensitivity, *Monthly Weather*  
541 *Review*, 129, 569-585, 2001.

542 Ciabatta, L., Camici, S., Brocca, L., Ponziani, F., Stelluti, M., Berni, N., and Moramarco, T. J. J.  
543 o. H.: Assessing the impact of climate-change scenarios on landslide occurrence in Umbria Region,  
544 *Italy*, 541, 285-295, 2016.

545 Crozier, M. J.: Prediction of rainfall-triggered landslides: A test of the antecedent water status  
546 model, *Earth surface processes and landforms*, 24, 825-833, 1999.

547 Dee, D. P., Uppala, S. M., Simmons, A., Berrisford, P., Poli, P., Kobayashi, S., Andrae, U.,  
548 Balmaseda, M., Balsamo, G., and Bauer, d. P.: The ERA-Interim reanalysis: Configuration and  
549 performance of the data assimilation system, *Quarterly Journal of the royal meteorological society*,  
550 137, 553-597, 2011.



551 Dorigo, W., Wagner, W., Albergel, C., Albrecht, F., Balsamo, G., Brocca, L., Chung, D., Ertl, M.,  
552 Forkel, M., and Gruber, A.: ESA CCI Soil Moisture for improved Earth system understanding:  
553 State-of-the art and future directions, *Remote Sensing of Environment*, 203, 185-215, 2017.

554 Dudhia, J.: Numerical study of convection observed during the winter monsoon experiment using  
555 a mesoscale two-dimensional model, *Journal of the Atmospheric Sciences*, 46, 3077-3107, 1989.

556 Ek, M., Mitchell, K., Lin, Y., Rogers, E., Grunmann, P., Koren, V., Gayno, G., and Tarpley, J.:  
557 Implementation of Noah land surface model advances in the National Centers for Environmental  
558 Prediction operational mesoscale Eta model, *Journal of Geophysical Research: Atmospheres*, 108,  
559 2003. DOI: <https://doi.org/10.1029/2002JD003296>.

560 Fawcett, T.: An introduction to ROC analysis, *Pattern recognition letters*, 27, 861-874, 2006.

561 Gariano, S. L., Brunetti, M. T., Iovine, G., Melillo, M., Peruccacci, S., Terranova, O., Vennari, C.,  
562 and Guzzetti, F.: Calibration and validation of rainfall thresholds for shallow landslide forecasting  
563 in Sicily, southern Italy, *Geomorphology*, 228, 653-665, 2015.

564 Gilliland, E. K., and Rowe, C. M.: A comparison of cumulus parameterization schemes in the  
565 WRF model, *Proceedings of the 87th AMS Annual Meeting & 21th Conference on Hydrology*,  
566 2007,

567 Glade, T., Crozier, M., and Smith, P.: Applying probability determination to refine landslide-  
568 triggering rainfall thresholds using an empirical “Antecedent Daily Rainfall Model”, *Pure and*  
569 *Applied Geophysics*, 157, 1059-1079, 2000.

570 Greve, P., Warrach-Sagi, K., and Wulfmeyer, V.: Evaluating soil water content in a WRF-Noah  
571 downscaling experiment, *Journal of Applied Meteorology and Climatology*, 52, 2312-2327, 2013.

572 Hawke, R., and McConchie, J.: In situ measurement of soil moisture and pore-water pressures in  
573 an ‘incipient’ landslide: Lake Tutira, New Zealand, *Journal of environmental management*, 92,  
574 266-274, 2011.

575 Hong, S.-Y., Noh, Y., and Dudhia, J.: A new vertical diffusion package with an explicit treatment  
576 of entrainment processes, *Monthly Weather Review*, 134, 2318-2341, 2006.

577 Hosmer, D., and Lemeshow, S.: Applied logistic regression. 1989, New York: Johns Wiley & Sons,  
578 1989.

579 Jiménez, P. A., Dudhia, J., González-Rouco, J. F., Navarro, J., Montávez, J. P., and García-  
580 Bustamante, E.: A revised scheme for the WRF surface layer formulation, Monthly Weather  
581 Review, 140, 898-918, 2012.

582 Jordan, R.: A one-dimensional temperature model for a snow cover: Technical documentation for  
583 SNTHERM. 89, Cold Regions Research and Engineering Laboratory, 1991.

584 Kain, J. S.: The Kain-Fritsch convective parameterization: An update, Journal of Applied  
585 Meteorology, 43, 2004. DOI: [http://dx.doi.org/10.1175/1520-  
586 0450\(2004\)043<0170:TKCPAU>2.0.CO;2](http://dx.doi.org/10.1175/1520-0450(2004)043<0170:TKCPAU>2.0.CO;2).

587 Klose, M., Highland, L., Damm, B., and Terhorst, B.: Estimation of Direct Landslide Costs in  
588 Industrialized Countries: Challenges, Concepts, and Case Study, in: Landslide Science for a Safer  
589 Geoenvironment, World Landslide Forum 3, China (Beijing), 2014, 661-667,

590 Lagomarsino, D., Segoni, S., Fanti, R., and Catani, F. J. L.: Updating and tuning a regional-scale  
591 landslide early warning system, 10, 91-97, 2013.

592 Lagomarsino, D., Segoni, S., Rosi, A., Rossi, G., Battistini, A., Catani, F., Casagli, N. J. N. H.,  
593 and Sciences, E. S.: Quantitative comparison between two different methodologies to define  
594 rainfall thresholds for landslide forecasting, 15, 2413-2423, 2015.

595 Lawrence, D. M., and Slater, A. G.: Incorporating organic soil into a global climate model, Climate  
596 Dynamics, 30, 145-160, 2008.

597 Lawrence, D. M., Oleson, K. W., Flanner, M. G., Thornton, P. E., Swenson, S. C., Lawrence, P.  
598 J., Zeng, X., Yang, Z. L., Levis, S., and Sakaguchi, K.: Parameterization improvements and  
599 functional and structural advances in version 4 of the Community Land Model, Journal of  
600 Advances in Modeling Earth Systems, 3, 27, 2011.

601 Lawrence, D. M., Oleson, K. W., Flanner, M. G., Fletcher, C. G., Lawrence, P. J., Levis, S.,  
602 Swenson, S. C., and Bonan, G. B.: The CCSM4 land simulation, 1850–2005: Assessment of  
603 surface climate and new capabilities, Journal of Climate, 25, 2240-2260, 2012.

604 Leung, L. R., and Qian, Y.: Atmospheric rivers induced heavy precipitation and flooding in the  
605 western US simulated by the WRF regional climate model, *Geophysical research letters*, 36, 2009.  
606 DOI: <https://doi.org/10.1029/2008GL036445>.

607 Liang, X., Xie, Z., and Huang, M.: A new parameterization for surface and groundwater  
608 interactions and its impact on water budgets with the variable infiltration capacity (VIC) land  
609 surface model, *Journal of Geophysical Research: Atmospheres*, 108, 2003. DOI:  
610 <https://doi.org/10.1029/2002JD003090>.

611 Maheu, A., Anctil, F., Gaborit, É., Fortin, V., Nadeau, D. F., and Therrien, R.: A field evaluation  
612 of soil moisture modelling with the Soil, Vegetation, and Snow (SVS) land surface model using  
613 evapotranspiration observations as forcing data, *Journal of Hydrology*, 558, 532-545, 2018.

614 Martelloni, G., Segoni, S., Fanti, R., and Catani, F. J. L.: Rainfall thresholds for the forecasting of  
615 landslide occurrence at regional scale, 9, 485-495, 2012.

616 Mlawer, E. J., Taubman, S. J., Brown, P. D., Iacono, M. J., and Clough, S. A.: Radiative transfer  
617 for inhomogeneous atmospheres: RRTM, a validated correlated-k model for the longwave, *Journal*  
618 *of Geophysical Research: Atmospheres*, 102, 16663-16682, 1997.

619 Niu, G. Y., Yang, Z. L., Dickinson, R. E., and Gulden, L. E.: A simple TOPMODEL-based runoff  
620 parameterization (SIMTOP) for use in global climate models, *Journal of Geophysical Research:*  
621 *Atmospheres*, 110, 2005. DOI: <https://doi.org/10.1029/2005JD006111>.

622 Niu, G. Y., Yang, Z. L., Dickinson, R. E., Gulden, L. E., and Su, H.: Development of a simple  
623 groundwater model for use in climate models and evaluation with Gravity Recovery and Climate  
624 Experiment data, *Journal of Geophysical Research: Atmospheres*, 112, 2007. DOI:  
625 <https://doi.org/10.1029/2006JD007522>.

626 Niu, G. Y., Yang, Z. L., Mitchell, K. E., Chen, F., Ek, M. B., Barlage, M., Kumar, A., Manning,  
627 K., Niyogi, D., and Rosero, E.: The community Noah land surface model with  
628 multiparameterization options (Noah-MP): 1. Model description and evaluation with local-scale  
629 measurements, *Journal of Geophysical Research: Atmospheres*, 116, 2011. DOI:  
630 <https://doi.org/10.1029/2010JD015139>.

631 Oleson, K., Niu, G. Y., Yang, Z. L., Lawrence, D., Thornton, P., Lawrence, P., Stöckli, R.,  
632 Dickinson, R., Bonan, G., and Levis, S.: Improvements to the Community Land Model and their  
633 impact on the hydrological cycle, *Journal of Geophysical Research: Biogeosciences* (2005–2012),  
634 113, 2008.

635 Oleson, K. W., Lawrence, D. M., Gordon, B., Flanner, M. G., Kluzek, E., Peter, J., Levis, S.,  
636 Swenson, S. C., Thornton, E., and Feddema, J.: Technical description of version 4.0 of the  
637 Community Land Model (CLM), 2010.

638 Pistocchi, A., Bouraoui, F., and Bittelli, M.: A simplified parameterization of the monthly topsoil  
639 water budget, *Water Resources Research*, 44, 2008. DOI: <https://doi.org/10.1029/2007WR006603>.

640 Ponziani, F., Pandolfo, C., Stelluti, M., Berni, N., Brocca, L., and Moramarco, T. J. L.: Assessment  
641 of rainfall thresholds and soil moisture modeling for operational hydrogeological risk prevention  
642 in the Umbria region (central Italy), 9, 229-237, 2012.

643 Posner, A. J., and Georgakakos, K. P.: Soil moisture and precipitation thresholds for real-time  
644 landslide prediction in El Salvador, *Landslides*, 12, 1179-1196, 2015.

645 Rossi, M., Witt, A., Guzzetti, F., Malamud, B. D., Peruccacci, S. J. E. S. P., and Landforms:  
646 Analysis of historical landslide time series in the Emilia-Romagna region, northern Italy, 35, 1123-  
647 1137, 2010.

648 Segoni, S., Lagomarsino, D., Fanti, R., Moretti, S., and Casagli, N.: Integration of rainfall  
649 thresholds and susceptibility maps in the Emilia Romagna (Italy) regional-scale landslide warning  
650 system, *Landslides*, 12, 773-785, 2015.

651 Segoni, S., Rosi, A., Fanti, R., Gallucci, A., Monni, A., and Casagli, N. J. W.: A Regional-Scale  
652 Landslide Warning System Based on 20 Years of Operational Experience, 10, 1297, 2018a.

653 Segoni, S., Rosi, A., Lagomarsino, D., Fanti, R., and Casagli, N.: Brief communication: Using  
654 averaged soil moisture estimates to improve the performances of a regional-scale landslide early  
655 warning system, *Natural Hazards and Earth System Sciences*, 18, 807-812, 2018b.

656 Skamarock, W., Klemp, J., Dudhia, J., Gill, D., Barker, D., Duda, M., Huang, X., Wang, W., and  
657 Powers, J.: A description of the advanced research WRF Version 3, NCAR technical note,

658 Mesoscale and Microscale Meteorology Division, National Center for Atmospheric Research,  
659 Boulder, Colorado, USA, 2008.

660 Skamarock, W. C., Klemp, J. B., Dudhia, J., Gill, D. O., Barker, D. M., Wang, W., and Powers, J.  
661 G.: A description of the advanced research WRF version 2, National Center For Atmospheric  
662 Research Boulder Co Mesoscale and Microscale Meteorology Div, 2005.

663 Srivastava, P. K., Han, D., Rico-Ramirez, M. A., Al-Shrafany, D., and Islam, T.: Data fusion  
664 techniques for improving soil moisture deficit using SMOS satellite and WRF-NOAH land surface  
665 model, *Water resources management*, 27, 5069-5087, 2013a.

666 Srivastava, P. K., Han, D., Rico Ramirez, M. A., and Islam, T.: Comparative assessment of  
667 evapotranspiration derived from NCEP and ECMWF global datasets through Weather Research  
668 and Forecasting model, *Atmospheric Science Letters*, 14, 118-125, 2013b.

669 Srivastava, P. K., Han, D., Rico-Ramirez, M. A., O'Neill, P., Islam, T., Gupta, M., and Dai, Q.:  
670 Performance evaluation of WRF-Noah Land surface model estimated soil moisture for  
671 hydrological application: Synergistic evaluation using SMOS retrieved soil moisture, *Journal of*  
672 *Hydrology*, 529, 200-212, 2015.

673 Stéfanon, M., Drobinski, P., D'Andrea, F., Lebeaupin-Brossier, C., and Bastin, S.: Soil moisture-  
674 temperature feedbacks at meso-scale during summer heat waves over Western Europe, *Climate*  
675 *dynamics*, 42, 1309-1324, 2014.

676 Temimi, M., Leconte, R., Chaouch, N., Sukumal, P., Khanbilvardi, R., and Brissette, F.: A  
677 combination of remote sensing data and topographic attributes for the spatial and temporal  
678 monitoring of soil wetness, *Journal of Hydrology*, 388, 28-40, 2010.

679 Thompson, G., Field, P. R., Rasmussen, R. M., and Hall, W. D.: Explicit forecasts of winter  
680 precipitation using an improved bulk microphysics scheme. Part II: Implementation of a new snow  
681 parameterization, *Monthly Weather Review*, 136, 5095-5115, 2008.

682 Tsai, T.-L., and Chen, H.-F.: Effects of degree of saturation on shallow landslides triggered by  
683 rainfall, *Environmental Earth Sciences*, 59, 1285-1295, 2010.

684 Valenzuela, P., Domínguez-Cuesta, M. J., García, M. A. M., and Jiménez-Sánchez, M.: Rainfall  
685 thresholds for the triggering of landslides considering previous soil moisture conditions (Asturias,  
686 NW Spain), *Landslides*, 15, 273-282, 2018.

687 Van Den Broeke, M. S., Kalin, A., Alavez, J. A. T., Oglesby, R., Hu, Q. J. T., and climatology, a.:  
688 A warm-season comparison of WRF coupled to the CLM4. 0, Noah-MP, and Bucket hydrology  
689 land surface schemes over the central USA, 134, 801-816, 2018.

690 Wei, J., Dirmeyer, P. A., Guo, Z., Zhang, L., and Misra, V.: How much do different land models  
691 matter for climate simulation? Part I: Climatology and variability, *Journal of Climate*, 23, 3120-  
692 3134, 2010.

693 Wharton, S., Simpson, M., Osuna, J., Newman, J., and Biraud, S.: Assessment of Land Surface  
694 Model Performance in WRF for Simulating Wind at Heights Relevant to the Wind Energy  
695 Community, Lawrence Livermore National Lab.(LLNL), Livermore, CA (United States), 2013.

696 Wilks, D.: *Statistical Methods in the Atmospheric Sciences*, 3rd ed., Academic Press, 2011.

697 Yang, Z. L., Niu, G. Y., Mitchell, K. E., Chen, F., Ek, M. B., Barlage, M., Longuevergne, L.,  
698 Manning, K., Niyogi, D., and Tewari, M.: The community Noah land surface model with  
699 multiparameterization options (Noah-MP): 2. Evaluation over global river basins, *Journal of*  
700 *Geophysical Research: Atmospheres*, 116, 2011.

701 Zaidi, S. M., and Gisen, J. I. A.: Evaluation of Weather Research and Forecasting (WRF)  
702 Microphysics single moment class-3 and class-6 in Precipitation Forecast, MATEC Web of  
703 Conferences, 2018, 03007,

704 Zaitchik, B. F., Santanello, J. A., Kumar, S. V., and Peters-Lidard, C. D.: Representation of soil  
705 moisture feedbacks during drought in NASA unified WRF (NU-WRF), *Journal of*  
706 *Hydrometeorology*, 14, 360-367, 2013.

707 Zeng, X., and Decker, M.: Improving the numerical solution of soil moisture-based Richards  
708 equation for land models with a deep or shallow water table, *Journal of Hydrometeorology*, 10,  
709 308-319, 2009.

710 Zhao, B., Dai, Q., Han, D., Dai, H., Mao, J., and Zhuo, L.: Antecedent wetness and rainfall  
711 information in landslide threshold definition, *Hydrol. Earth Syst. Sci. Discuss.*, 2019, 1-26,  
712 10.5194/hess-2019-150, 2019a.

713 Zhao, B., Dai, Q., Han, D., Dai, H., Mao, J., and Zhuo, L. J. J. o. H.: Probabilistic thresholds for  
714 landslides warning by integrating soil moisture conditions with rainfall thresholds, *574*, 276-287,  
715 2019b.

716 Zhuo, L., Dai, Q., and Han, D.: Evaluation of SMOS soil moisture retrievals over the central United  
717 States for hydro-meteorological application, *Physics and Chemistry of the Earth, Parts A/B/C*, 83,  
718 146-155, 2015a.

719 Zhuo, L., Han, D., Dai, Q., Islam, T., and Srivastava, P. K.: Appraisal of NLDAS-2 multi-model  
720 simulated soil moistures for hydrological modelling, *Water resources management*, 29, 3503-3517,  
721 2015b.

722 Zhuo, L., Dai, Q., Han, D., Chen, N., Zhao, B., and Berti, M.: Evaluation of remotely sensed soil  
723 moisture for landslide hazard assessment, *IEEE Journal of Selected Topics in Applied Earth  
724 Observations and Remote Sensing*, 12, 162 - 173, 2019.

725

**Table 1.** Comparison of Noah, Noah-MP, and CLM4.

	Noah	Noah-MP	CLM4
Energy balance	Yes	Yes	Yes
Water balance	Yes	Yes	Yes
No. of soil layers	4	4	10
Depth of total soil column	2.0 m	2.0 m	3.802 m
Model soil layer thickness	0.1, 0.3, 0.6, 1.0 m	0.1, 0.3, 0.6, 1.0 m	0.018, 0.028, 0.045, 0.075, 0.124, 0.204, 0.336, 0.553, 0.913, 1.506 m
No. of vegetation layers	A single combined surface layer of vegetation and snow	Single layer	Single layer
Vegetation	Dominant vegetation type in one grid cell with prescribed LAI	Dominant vegetation type in one grid cell with dynamic LAI	Up to 10 vegetation types in one grid cell with prescribed LAI
No. of snow layers	A single combined surface layer of vegetation and snow	Up to three layers	Up to five layers



**Table 2.** WRF parameterizations used in this study.

	Settings/ Parameterizations	References
Map projection	Lambert	
Central point of domain	Latitude: 44.54; Longitude: 11.02	
Latitudinal grid length	5 km	
Longitudinal grid length	5 km	
Model output time step	Daily	
Nesting	Two-way	
Land surface model	Noah, Noah-MP, CLM	
Simulation period	1/1/2006 – 31/12/2015	
Spin-up period	1/1/2005 – 31/12/2005	
Microphysics	New Thompson	(Thompson et al., 2008)
Shortwave radiation	Dudhia scheme	(Dudhia, 1989)
Longwave radiation	Rapid Radiative Transfer Model	(Mlawer et al., 1997)
Surface layer	Revised MM5	(Jiménez et al., 2012; Chen and Dudhia, 2001)
Planetary boundary layer	Yonsei University method	(Hong et al., 2006)
Cumulus Parameterization	Kain-Fritsch (new Eta) scheme	(Kain, 2004)

**Table 3.** Statistical summary of the WRF performance in simulating soil moisture for different soil layers, based on comparison with the single point in-situ observations.

	<i>R</i>				<i>RMSE (m<sup>3</sup>/m<sup>3</sup>)</i>			
	0.10 m	0.25 m	0.70 m	1.50 m	0.1 m	0.25 m	0.70 m	1.50 m
Noah	0.728	0.645	0.660	0.430	0.123	0.125	0.141	<b>0.055</b>
Noah-MP	<b>0.809</b>	0.683	<b>0.738</b>	<b>0.498</b>	<b>0.060</b>	<b>0.070</b>	<b>0.088</b>	0.092
CLM	0.789	<b>0.743</b>	0.648	0.287	0.089	0.087	0.123	0.089

**Table 4.** Statistical summary of the WRF performance in simulating rainfall for the whole study region, based on comparison with the in-situ rainfall network.

	<i>R</i>			<i>RMSE (mm)</i>		
	Noah	Noah-MP	CLM4	Noah	Noah-MP	CLM4
Min	0.094	0.090	0.076	4.275	4.286	4.219
Max	0.779	0.798	0.801	19.814	19.178	19.476
Mean	0.425	0.426	0.421	7.772	7.719	7.943
0.25 percentile	0.147	0.130	0.154	4.579	4.297	4.438
0.50 percentile	0.189	0.153	0.210	4.951	4.909	4.910
0.75 percentile	0.192	0.183	0.211	5.006	4.970	5.010

**Table 5.** Rainfall events information.

Starting date			Ending date			Duration (days)	Rainfall intensity (mm/day)	Number of Landslide events
Year	Month	Day	Year	Month	Day			
2014	1	13	2014	1	24	12	20.50	2
2014	1	28	2014	2	14	18	13.61	0
2014	2	26	2014	3	6	9	13.35	0
2014	3	22	2014	3	27	6	11.08	0
2014	4	4	2014	4	5	2	18.98	0
2014	4	27	2014	5	4	8	12.13	0
2014	5	26	2014	6	3	9	5.05	0
2014	6	14	2014	6	16	3	18.29	0
2014	6	25	2014	6	30	6	11.39	0
2014	7	7	2014	7	14	8	7.84	0
2014	7	21	2014	7	30	10	15.35	0
2014	8	31	2014	9	5	6	5.67	0
2014	9	10	2014	9	12	3	11.84	0
2014	9	19	2014	9	20	2	23.04	0
2014	10	1	2014	10	1	1	14.51	0
2014	10	10	2014	10	17	8	13.01	0
2014	11	4	2014	11	18	15	18.28	0
2014	11	25	2014	12	7	13	7.58	0
2014	12	13	2014	12	16	4	6.24	0
2015	1	16	2015	1	17	2	14.87	0
2015	1	21	2015	1	23	3	7.13	0
2015	1	29	2015	2	10	13	9.98	0
2015	2	13	2015	2	17	5	6.62	1
2015	2	21	2015	2	26	6	11.84	4
2015	3	3	2015	3	7	5	11.69	1
2015	3	15	2015	3	17	3	9.00	0
2015	3	21	2015	3	27	7	12.09	2
2015	4	3	2015	4	5	3	16.62	0
2015	4	17	2015	4	18	2	6.99	0
2015	4	26	2015	4	29	4	11.23	0
2015	5	15	2015	5	16	2	8.83	0
2015	5	20	2015	5	27	8	10.58	1
2015	6	8	2015	6	11	4	6.47	0
2015	6	16	2015	6	19	4	13.44	0
2015	6	23	2015	6	24	2	6.07	0
2015	7	22	2015	7	25	4	6.05	0
2015	8	9	2015	8	10	2	24.69	0
2015	8	15	2015	8	19	5	10.69	0
2015	8	23	2015	8	24	2	7.88	0
2015	9	13	2015	9	14	2	24.66	1
2015	9	23	2015	9	24	2	7.50	0
2015	10	1	2015	10	7	7	13.73	0
2015	10	10	2015	10	19	10	9.40	0
2015	10	27	2015	10	29	3	20.33	0
2015	11	21	2015	11	25	5	13.78	1

**Table 6.** Results of Euclidean distances ( $d$ ) between individual points and the optimal point for ROC analysis are listed. The best performance (i.e., lowest  $d$ ) for each column (i.e., each soil layer of an LSM scheme) is highlighted. The optimal performance of all is highlighted in red.

<i>e.p.</i> (%)	Noah				Noah-MP				CLM4			
	10 cm	25 cm	70 cm	150 cm	10 cm	25 cm	70 cm	150 cm	10 cm	25 cm	70 cm	150 cm
1	0.942	0.971	0.962	0.947	0.857	0.937	0.897	0.963	0.942	0.939	0.978	0.975
2	0.906	0.945	0.963	0.923	0.854	0.912	0.883	0.959	0.923	0.922	0.959	0.952
3	0.889	0.924	0.961	0.915	0.849	0.855	0.838	0.952	0.870	0.874	0.940	0.947
4	0.884	0.898	0.946	0.914	0.838	0.814	0.829	0.924	0.831	0.843	0.925	0.947
5	0.860	0.875	0.924	0.896	0.820	0.793	0.812	0.908	0.791	0.822	0.915	0.921
6	0.835	0.854	0.910	0.874	0.803	0.785	0.800	0.905	0.770	0.817	0.911	0.909
7	0.827	0.861	0.902	0.858	0.777	0.767	0.791	0.889	0.753	0.801	0.902	0.900
8	0.816	0.849	0.889	0.851	0.745	0.765	0.782	0.876	0.745	0.785	0.902	0.910
9	0.790	0.827	0.878	0.834	0.706	0.732	0.766	0.871	0.742	0.777	0.864	0.904
10	0.762	0.811	0.863	0.825	0.672	0.702	0.747	0.862	0.738	0.767	0.835	0.887
15	0.615	0.741	0.839	0.763	0.560	0.629	0.716	0.835	0.702	0.700	0.729	0.790
20	0.485	0.627	0.779	0.652	0.515	0.571	0.624	0.774	0.570	0.602	0.594	0.650
25	0.432	0.544	0.728	0.512	0.403	0.465	0.574	0.736	0.509	0.522	0.471	0.509
30	0.437	0.495	0.643	0.451	<b>0.369</b>	<b>0.375</b>	0.544	0.679	0.475	0.477	0.447	0.469
35	<b>0.392</b>	0.446	0.592	0.436	0.390	0.404	0.411	0.498	0.441	0.435	0.428	0.430
40	0.500	<b>0.407</b>	0.531	0.416	0.439	0.385	<b>0.382</b>	0.436	<b>0.406</b>	<b>0.405</b>	<b>0.398</b>	<b>0.410</b>
50	0.552	0.425	<b>0.404</b>	<b>0.411</b>	0.489	0.417	0.416	<b>0.429</b>	0.437	0.435	0.408	0.437

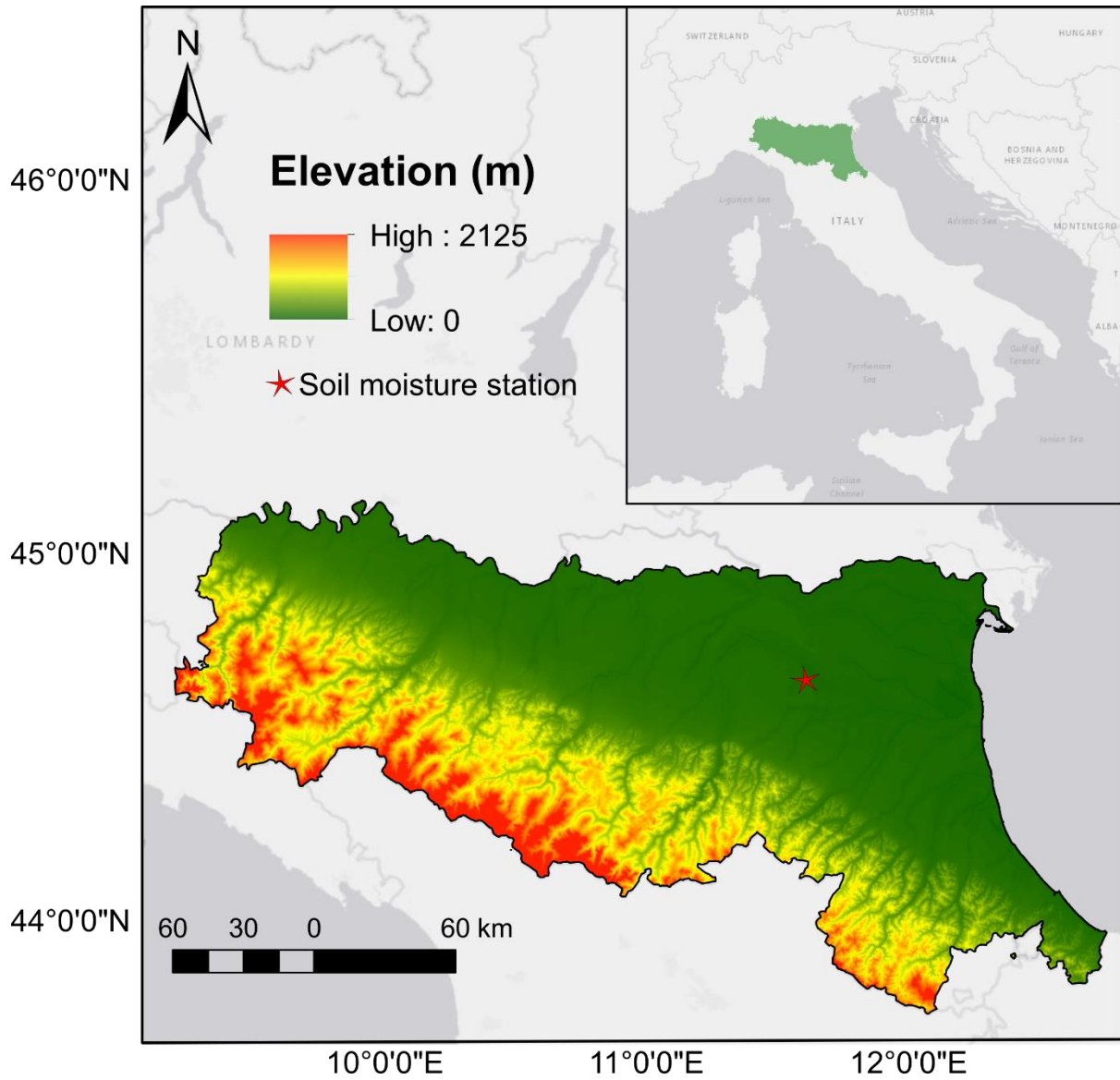


**Figure 1.** Location of the Emilia Romagna Region with elevation map and in-situ soil moisture station also shown.

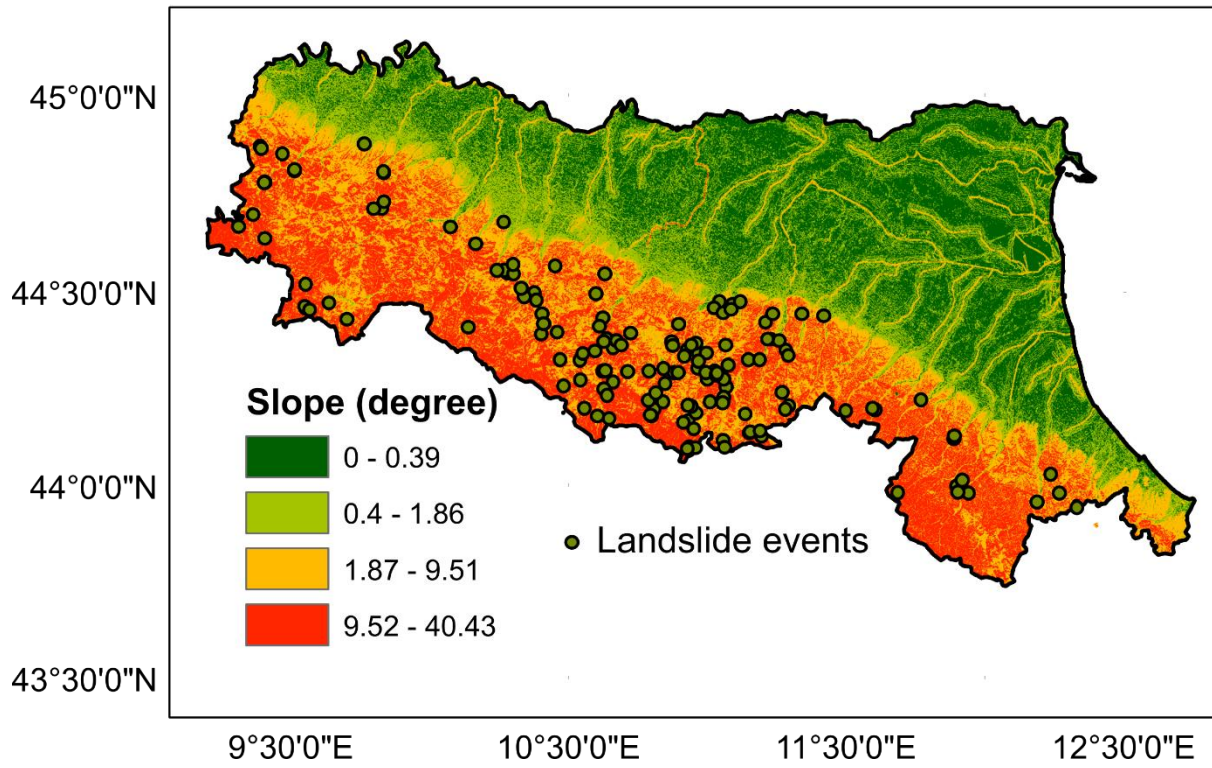


**Figure 2.** Landslide events with slope angle map.

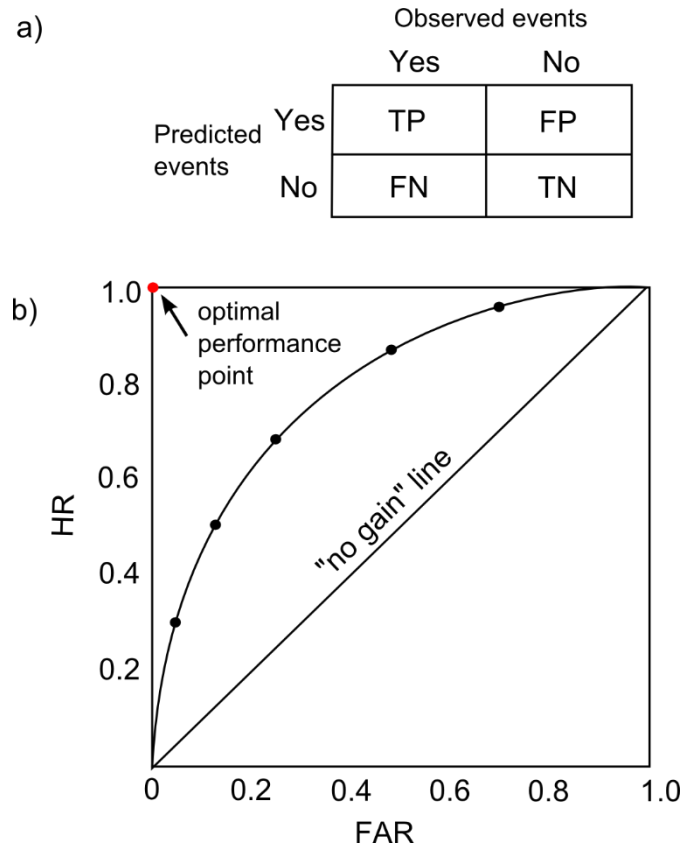


**Figure 3.** a) Contingency table illustrates the four possible outcomes of a binary classifier model: TP (True Positive), TN (True Negative), FP (False Positive), and FN (False Negative). b) ROC (Receiver Operating Characteristic) analysis with HR (Hitting Rate) against FAR (False Alarm Rate).



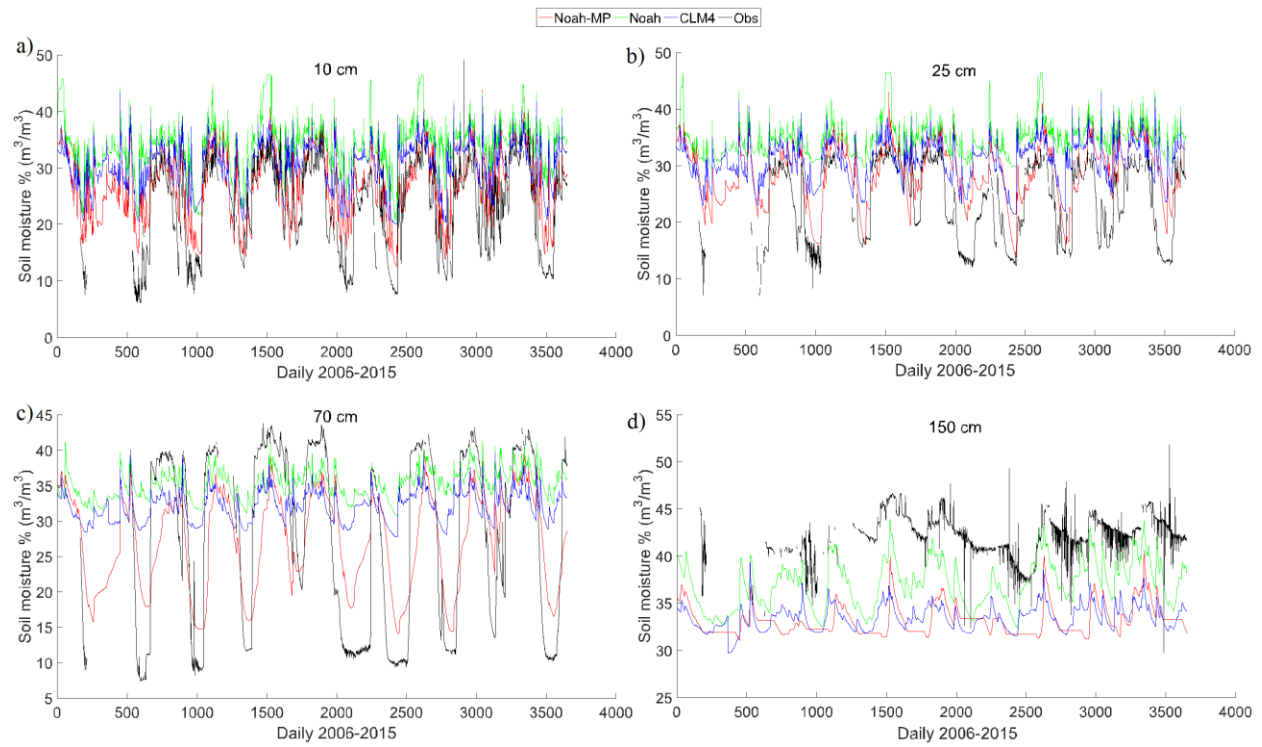


**Figure 4.** Soil moisture temporal variations of WRF simulations and in-situ observations for four soil layers at a) 10 cm; b) 25 cm; c) 70 cm; and d) 150 cm.

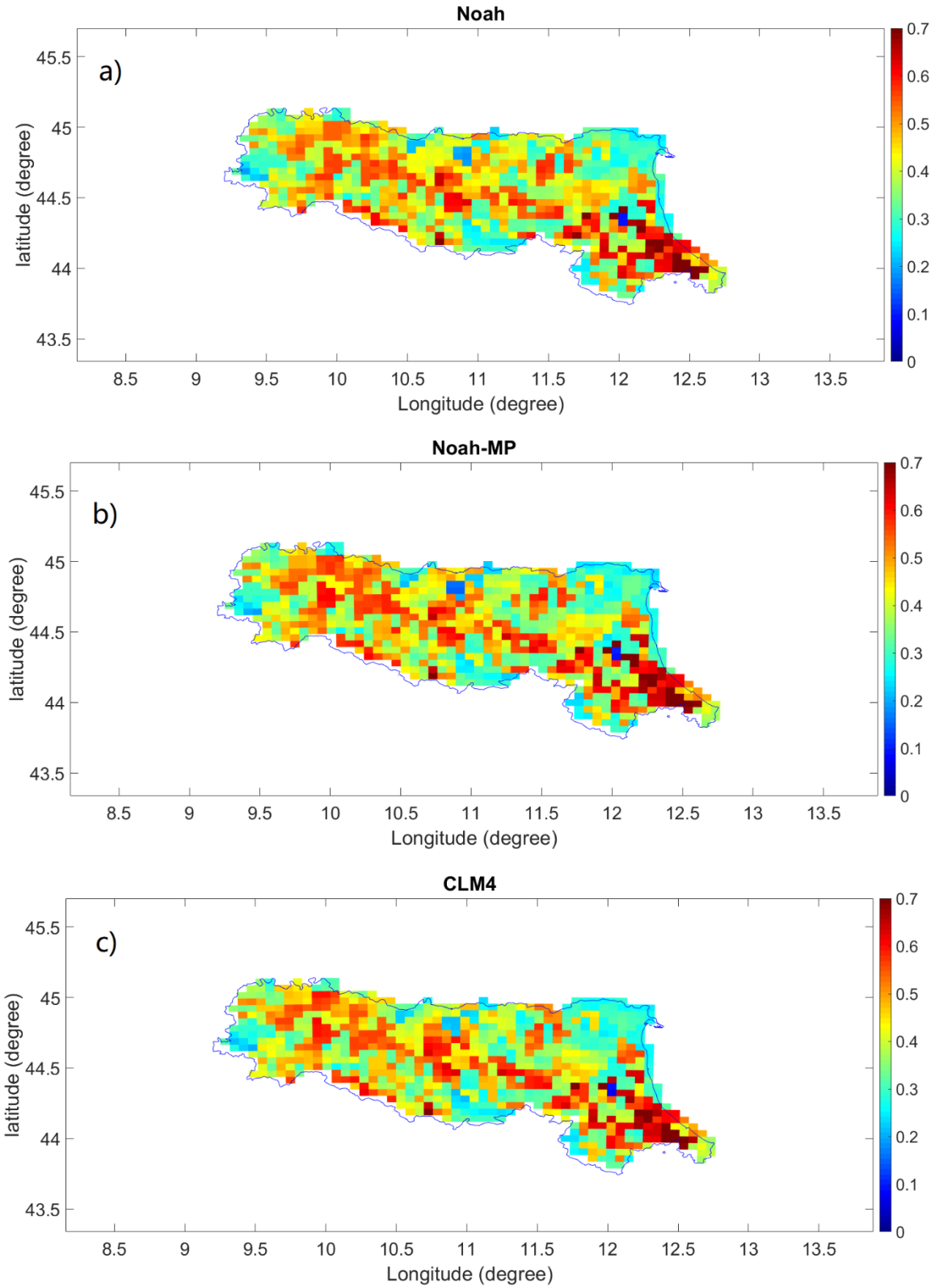


**Figure 5.** Rainfall evaluation: spatial distribution of the correlation coefficient  $R$  of a) Noah, b) Noah-MP and c) CLM4.

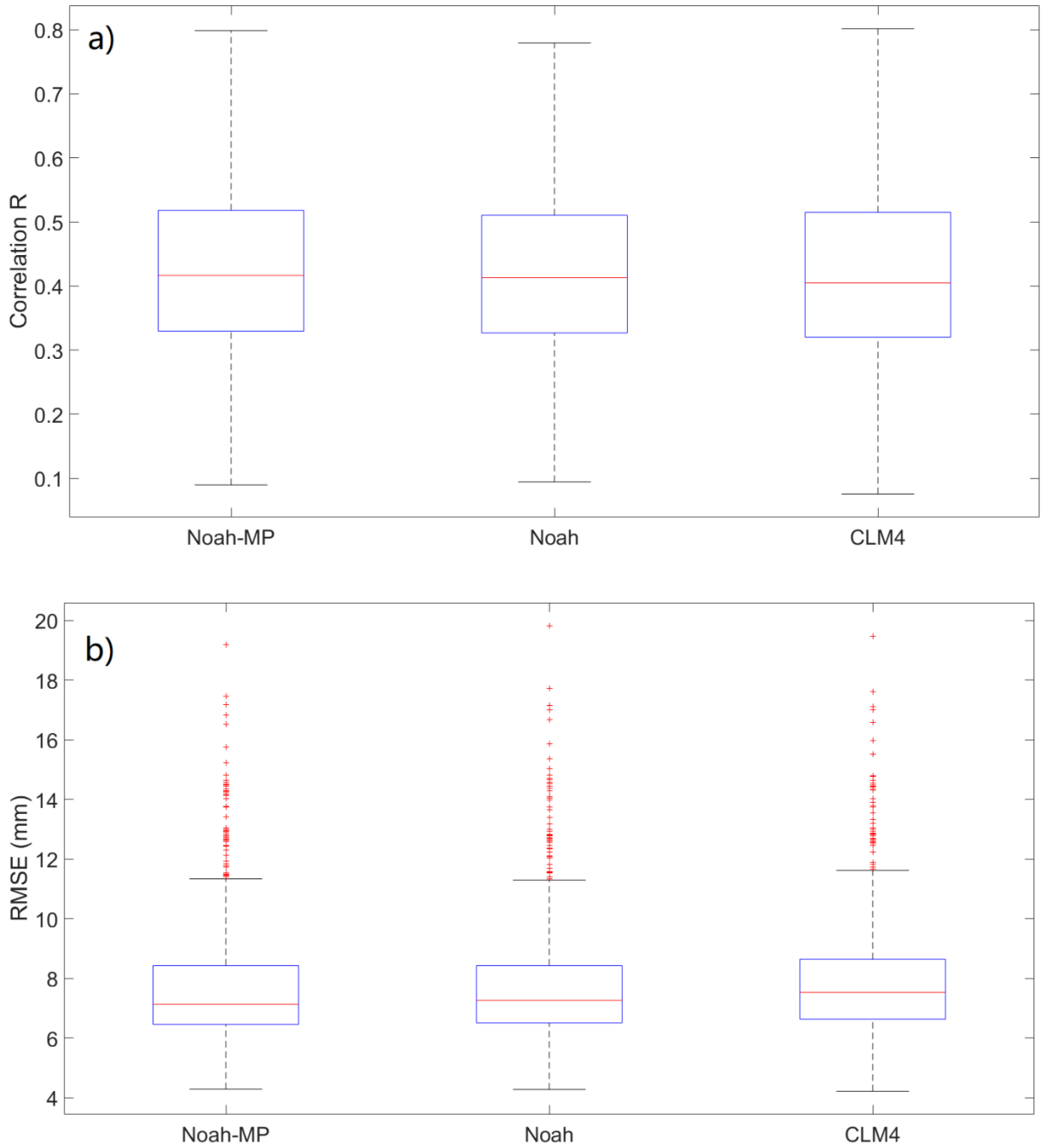


**Figure 6.** Boxplots of rainfall evaluation results of a)  $R$  and b)  $RMSE$ : minimum, maximum, 0.25, 0.50 and 0.75 percentiles, and outliers (red cross).

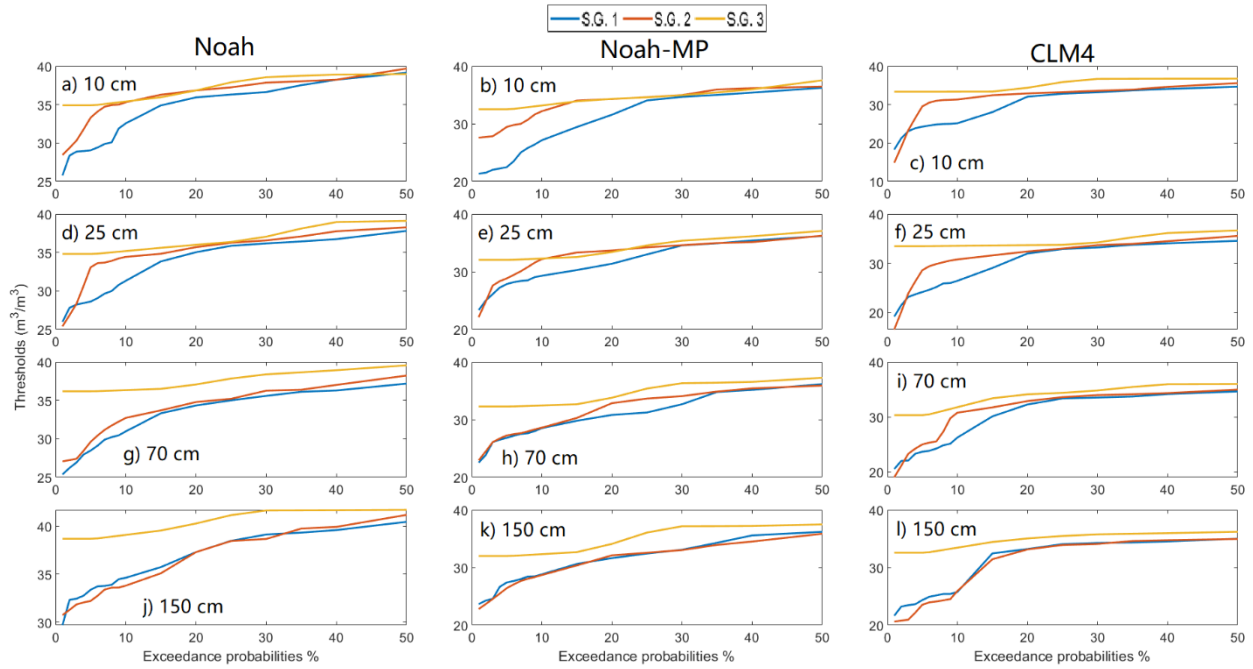


**Figure 7.** Threshold plots. For Noah (a, d, g, j), Noah-MP (b, e, h, k), and CLM4 (c, f, i, l) land surface schemes under three Slope angle Groups (S.G.) with S.G. 1 = 0.4-1.86°; S.G. 2 = 1.87-9.61°; S.G. 3 = 9.52-40.43°.

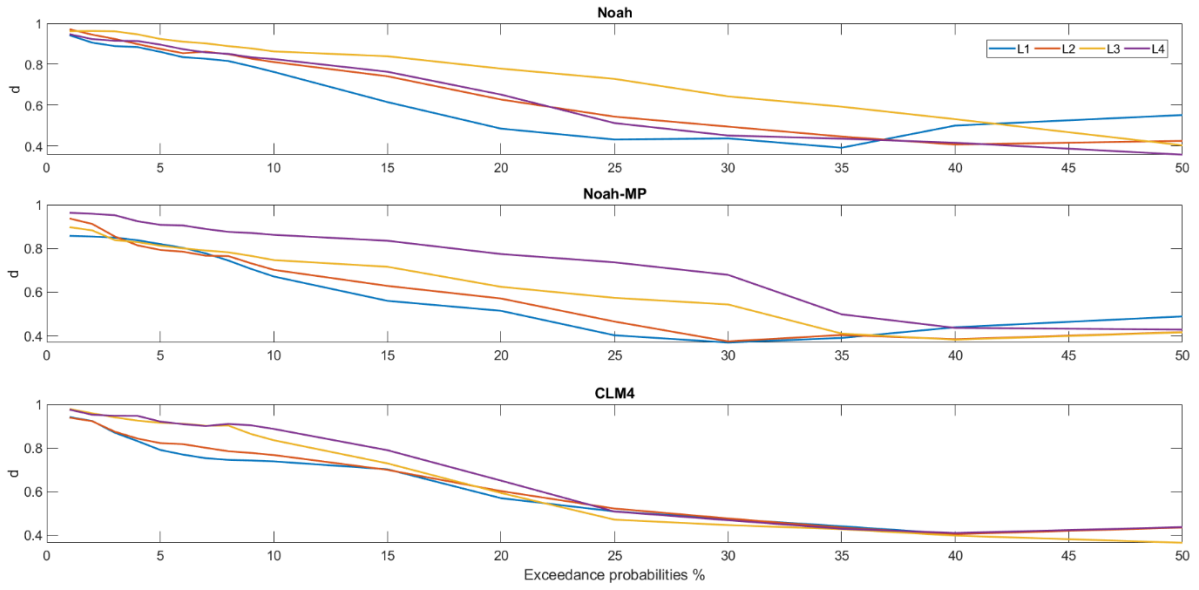


**Figure 8.** d-scores.

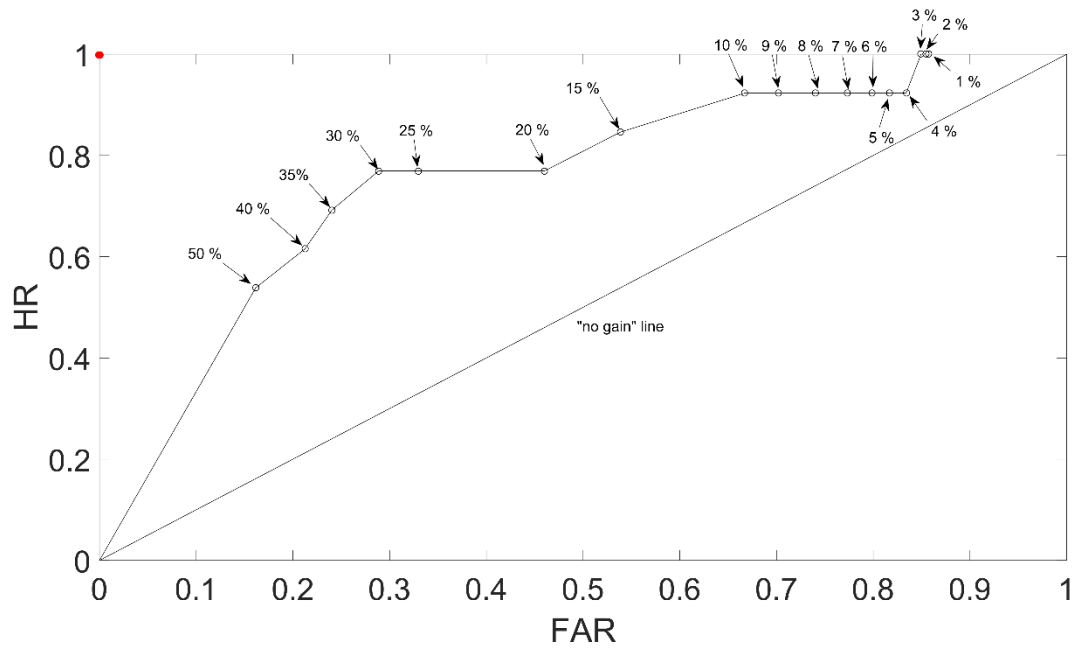


**Figure 9.** ROC curve for the calculated thresholds using different exceedance probability levels (for Noah-MP at the surface layer). The *no gain* line and the optimal performance point (the red point) are also presented.